High-resolution under-water laser spectrometer sensing provides new insights to methane distribution at an Arctic seepage site

Pär Jansson[1], Jack Triest[2], Roberto Grilli[2], Bénédicte Ferré[1], Anna Silyakova[1], Jürgen Mienert[1], Jérôme Chappellaz[2]

[1] CAGE Center for Arctic Gas Hydrate, Environment, and Climate, Department of Geosciences, UiT-The Arctic University of Norway, 9037, Tromsø, Norway

5   [2] Univ. Grenoble Alpes, CNRS, IRD, Grenoble INP, IGE, 38000 Grenoble, France

Correspondence to: Pär Jansson (per.g.jansson@uit.no), Roberto Grilli (roberto.grilli@cnrs.fr)

1

Abstract. Methane (CH$_4$) in marine sediments has the potential to contribute to changes in the ocean- and climate system. Physical and biochemical processes that are difficult to quantify with current standard methods such as acoustic surveys and discrete sampling govern the distribution of dissolved CH$_4$ in oceans and lakes. Detailed observations of aquatic CH$_4$ concentrations are required for a better understanding of CH$_4$ dynamics in the water column, how it can affect lake- and ocean acidification, the chemosynthetic ecosystem, and mixing ratios of atmospheric climate gases. Here we present pioneering high-resolution in-situ measurements of dissolved CH$_4$ throughout the water column over a 400 m deep CH$_4$ seepage area at the continental slope west of Svalbard. A new fast-response under-water membrane-inlet laser spectrometer sensor demonstrates technological advances and breakthroughs for ocean measurements. We reveal decametre-scale variations of dissolved CH$_4$ concentrations over the CH$_4$ seepage zone. Previous studies could not resolve such heterogeneity in the area, assumed smoother distribution and therefore lacked both details and insights to ongoing processes. We show good repeatability of the instrument measurements, which are also in agreement with discrete sampling. New numerical models, based on acoustically evidenced free gas emissions from the seafloor, support the observed heterogeneity and CH$_4$ inventory. We identified sources of CH$_4$, undetectable with echosounder, and rapid diffusion of dissolved CH$_4$ away from the sources. Results from the continuous ocean laser-spectrometer measurements, supported by modelling, improve our understanding of CH$_4$ fluxes and related physical processes over Arctic CH$_4$ degassing regions.

1 Introduction

Methane (CH$_4$) release from gas bearing ocean sediments has been of high interest for many years (e.g. Westbrook et al., 2009;Ferré et al., 2012;Ruppel and Kessler, 2016;Jørgensen et al., 1990;Boetius and Wenzhöfer, 2013;Myhre et al., 2016;Platt et al., 2018). Once released and dissolved in the water column, the CH$_4$ gas diffuses and is partly oxidized in the water column (Reeburgh, 2007), contributing to minimum oxygen zones (Boetius and Wenzhöfer, 2013) and possibly to ocean acidification (Biastoch et al., 2011). Chemosynthetic life on the seabed depends on the supply of methane as an energy resource (e.g. Boetius and Wenzhöfer, 2013). Supply of nutrient rich bottom water, by means of local upwelling, may enhance biological productivity, induce drawdown of CO$_2$ from the atmosphere, potentially making shallow CH$_4$ seepage sites sinks for this critical greenhouse gas (Pohlman et al., 2017). Warming of ocean bottom waters, active tectonics and ice sheet build up and retreat could, at different time scales, lead to CH$_4$ gas release from the seabed (e.g. Portnov et al., 2016). The magnitude and trend of such a phenomena are still under debate (e.g. Hong et al., 2018;Ruppel and Kessler, 2016;Andreassen et al., 2017) and accurate methods to measure methane concentration from its source are needed. At shallow seepage sites, such as the East Siberian Arctic Shelf, CH$_4$ can potentially reach the atmosphere and amplify greenhouse warming (Shakhova et al., 2010;Shakhova et al., 2014). However, most studies of shallow CH$_4$ seepage sites have found no or little CH$_4$ flux to the atmosphere (e.g. Miller et al., 2017;Platt et al., 2018;Myhre et al., 2016;Gentz et al., 2014).

In the past, most CH_4 measurements relied on indirect or discrete sample measurements (e.g. Damm et al., 2005;Westbrook et al., 2009;Gentz et al., 2014). Bubble catcher and mapping with multibeam echosounder (Sahling et al., 2014), hydro-acoustic imaging together with bubble size and bubble rising speed measurements (Sahling et al., 2014;Weber et al., 2014;Veloso et al., 2015;Greinert et al., 2006;Ostrovsky, 2003) have been used to derive CH_4 flow rates. The acoustic method effectively maps CH_4 seepage from acoustically detectable sources, and camera equipped ROVs can investigate their properties. However, these methods cannot detect CH_4 from sources other than free gas seepage and do not provide information about the distribution of dissolved CH_4. Discrete sampling with Niskin bottles allows 3D mapping of dissolved CH_4, but is limited by its labour intense nature, with resulting low resolution, which in turn may lead to smoothing and inaccurate estimates of CH_4 inventories. The combination of bubble catcher and multibeam echosounder is very efficient once the bubble seepage has been properly categorised, but uncertainties arise while extrapolating bubble catcher flow rates to acoustically evidenced bubble streams (flares). Present commercial underwater CH_4 sensors do not have the required response time for accurate high-resolution mapping. For this reason, Gentz et al. (2014) deployed an underwater membrane inlet mass spectrometer (UWMS) with a fast response time for mapping of CH_4 at shallow (10 m) depths. Boulart et al. (2013) used an in-situ, real time sensor in the Baltic Sea. The instrument response time of 1–2 minutes and detection limit of 3 nmol l^{-1} represent limitations for fast profiling and near surface concentration studies linked to atmospheric exchange. Sommer et al. (2015) used a pump-fed membrane inlet mass spectrometry installation at a blowout location in the North Sea. They achieved a response time of 30 minutes and a detection limit of 20 nmol l^{-1}. Wankel et al. (2010), deployed a deep-sea graded in-situ mass spectrometer over a brine pool in the gulf of Mexico, where they measured high (μM – mM) concentrations of CH_4. They do not specify their detection limit or the response time of the instrument, but state an uncertainty of 11%. Boulart et al. (2017) mapped hydrothermal activity while deploying an in-situ mass spectrometer (ISMS) over the southeast Indian Ridge. The ISMS has the advantage of measuring several dissolved gases simultaneously, but only CH_4 was reported because of the high detection limit of H_2. The ISMS response time and detection limits were not specified.

Here we present the first in-situ, high-resolution ocean laser spectroscopy mapping of dissolved CH_4 in seawater over active CH_4 seepage in the Arctic. The data was collected by deploying a patent based (Triest et al. patent France No. 17 50063) membrane inlet laser spectrometer (MILS) (Grilli et al., 2018). The high-resolution measurements, together with echosounder data, discrete water sampling, and newly developed control volume and 2-dimensional (2D) models improve our understanding of CH_4 fluxes from the seabed into oceans and lakes, and potentially to the atmosphere.

2 Materials and methods

2.1 Study area

The survey was performed on board RV Helmer Hanssen, UiT, The Arctic University of Norway, in October 2015 (CAGE 15-6 cruise) west of Prins Karls Forland located offshore western Svalbard. Over a period of three days (October 21–23), we

3

70 surveyed an area of ~18 km^2 at water depths between 350 and 420 m, using continuous under-water laser spectroscopy as well as traditional discrete sampling for dissolved CH_4, and echosounding for bubble detection and gas seepage quantification. The study area is located at 78°33´ N, 9°30´ E over an active CH_4 venting area (Fig. 1a). Here, more than 250 flares (acoustic signature of bubble streams in echograms) exist along the shelf break (e.g. Sahling et al., 2014;Westbrook et al., 2009;Damm et al., 2005;Graves et al., 2015;Berndt et al., 2014). The northward flowing West Spitsbergen Current (WSC), which transports

75 Atlantic Water (AW, S>34.9, T>3° C) (Schauer et al., 2004), controls the hydrography of the study area. The East Spitsbergen Current (ESC), flows south-westward along the eastern Spitsbergen coast, and northward along the western Svalbard margin, carrying Arctic Surface Water (ASW, 34.4⩽S⩽34.9) and Polar Water (PW, S<34.4) (Skogseth et al., 2005). The Coastal Current (CC), extension of the ESC (Loeng, 1991;Skogseth et al., 2005), contributes a transient addition of ASW and PW on the shelf and the continental slope as the WSC meanders on- and offshore (Steinle et al., 2015). The Lower Arctic Intermediate

80 Water (LAIW, S>34.9, T⩽3 °C) flows below the Atlantic Water (Ślubowska-Woldengen et al., 2007).

2.2 Hydrocasts with discrete water sampling

Vertical oceanographic profiles were recorded at 10 stations (Fig. 1a) using a Seabird SBE 911 plus CTD (Conductivity, Temperature, and Depth) mounted on a rosette, which carried twelve 5-liter Niskin bottles. In January 2015, the CTD was fitted with new sensors. An SBE 4 Conductivity Sensor and an SBE 3plus Premium CTD Temperature Sensor, with initial

85 accuracies of ± 0.001 °C and ± 0.3 mS m^{-1}. At 24 Hz sampling, the resolutions are 0.0003 °C and 0.04 mS m^{-1}.

The Niskin bottles were closed during the up-casts, collecting seawater at different depths for further dissolved CH_4 analysis. Headspace equilibration followed by gas chromatography (GC) analysis was carried out in the laboratory at the Department of Geoscience at UiT, The Arctic University of Norway, using the same technique as Grilli et al. (2018). The resulting headspace mixing ratios (ppmv) were converted to in-situ concentrations (nmol l^{-1}), using Henry's solubility law, with

90 coefficients calculated accordingly with Wiesenburg and Guinasso (1979). The sample dilution from addition of a reaction stopper (1 ml of 1M NaOH solution replacing 1 ml of each 120 ml sample), and the removal of sample water while introducing headspace gas (5 ml of pure N_2 replacing 5 ml of sample water) was accounted for. The overall error for the headspace GC method was 4%, based on standard deviation of replicates.

2.3 Methodology and technology for high-resolution laser spectrometer CH_4 sensing

95 A stainless steel frame attached to a cable connected to an on-board winch served as a platform to which the MILS, an Aanderaa, Seaguard TD262a CTD, a standard commercial CH_4 sensor, and a battery pack were mounted. This instrument assembly, hereafter called "probe", has a total height of ~1.8 m, a total weight in air of ~160 kg and a negative buoyancy of ~52 kg. We towed the probe for a total of 28 hours, providing unsurpassed high-resolution in-situ CH_4 measurements with a sampling rate of 1 s^{-1}, together with dissolved oxygen data, as well as pressure, temperature and salinity. The autonomy of

100 the MILS was ~12 hours at 50 W power consumption. The sensors fitted to the Aanderaa CTD, a Conductivity Sensor 4319,

4

a Temperature Sensor 4060, and an Oxygen Optode 4330, has initial accuracies of $\pm 0.03°C$, ± 5 mS m^{-1}, and $< \pm 8$ µM and resolutions of 0.001 °C, 0.2 mS m^{-1}, and < 1 µM, respectively.

Lowering and heaving of the probe in the water column allowed for vertical casts, while towing the probe behind the moving ship at varying heights above the seafloor generated near-horizontal trajectories. The main horizontal trajectories, acquired at a ship speed of 1.5 ± 0.15 knots, comprise five lines (Fig. 1a), where the desired distance from the seafloor was attained by monitoring the pressure in real time while adjusting the cable payout. The battery-powered MILS (Fig. 1b, see Grilli et al. (2018) for more details) has a membrane inlet system, linked to an optical feedback cavity-enhanced absorption spectrometer and an integrated PC for control and data storage. Cabled real-time communication with the instruments allowed instant decision-making, and ensuring optimal sensor operation during the deployments.
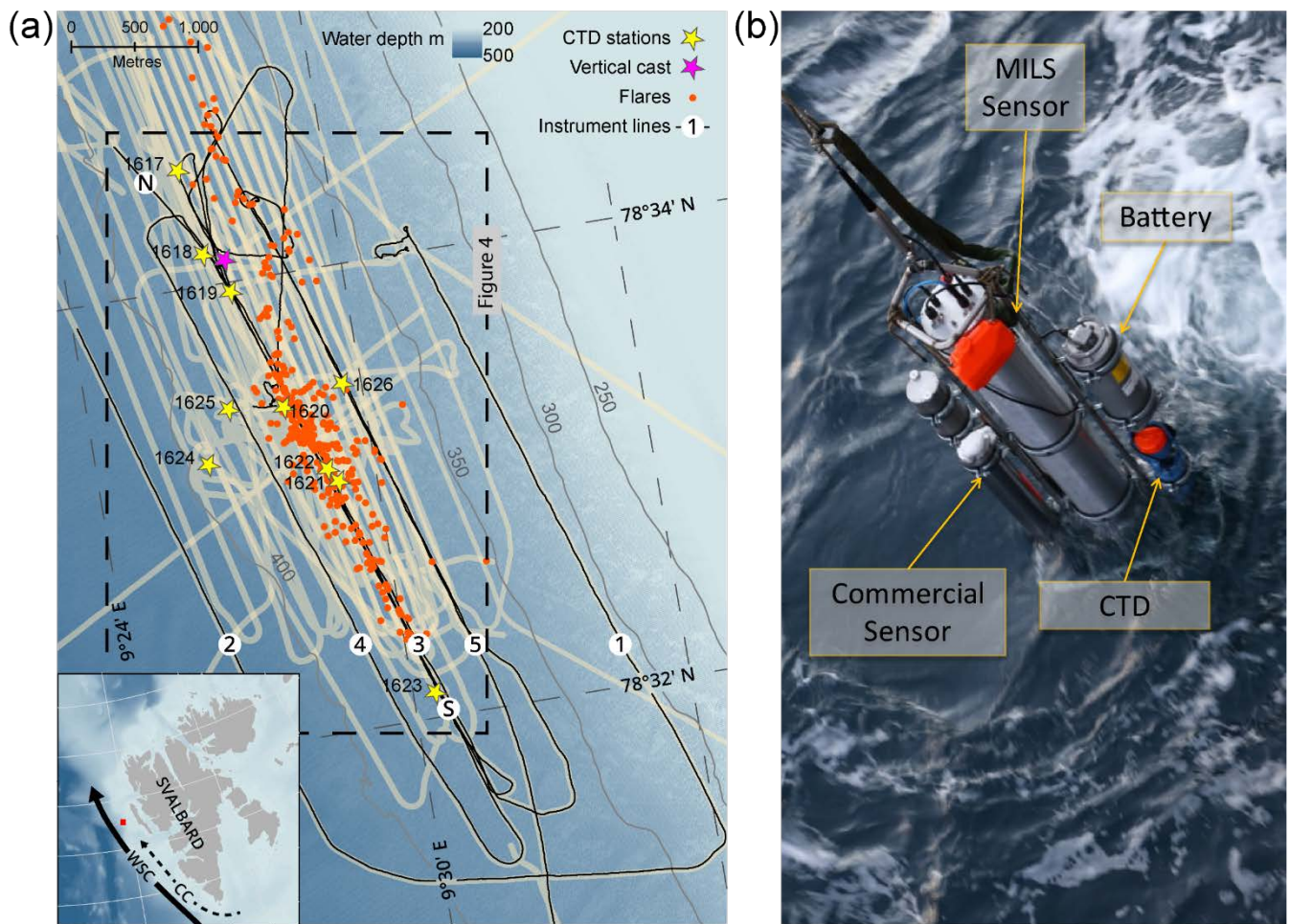
Figure 1: Map of the surveyed area and photo of the instrument assembly. a) Survey lines and sampling locations over the study area at the Svalbard continental margin. Black lines show the ship trajectory with line numbers assigned in the order they were surveyed. Beige areas appearing as thick lines indicate echosounder beam coverage from this campaign and previous cruises (AOEM 2010, and CAGE 13-7 in 2013). The start- and end- locations of line 3 are indicated with N and S respectively. Known flare locations from this survey and surveys in 2010 and 2013 are marked with orange dots. CTD stations with discrete water sampling are marked with yellow stars and the vertical instrument cast with a purple star. The inset image shows an overview of Svalbard with the survey location indicated with a red square. The controlling currents are shown with solid (WSC) and dashed (Coastal current) black lines. b) Instrument assembly. The main central tube is the prototype MILS sensor. The stainless steel frame acts as a platform and allows attachment of instrument battery (top right side), CTD (blue at the bottom right) and a commercial CH$_4$ sensor and its battery pack (left side).

Sensors with membrane inlets can be sensitive to fluctuating water flow over the membrane, which can result in artificial variability of measured concentrations. The SBE5T pump was positioned about 25cm away from the membrane inlets and connected with short ½" hose sections and a T piece. By shielding the inlet and outlets and mounting them at the same height with an open flow-path, pressure changes due to movement through the water column were minimised. The water pump inlet has a fine mesh filter and a shield to avoid entry of free gas bubbles and artefacts from gas bubbles entering the sampling unit and reaching the membrane surface.

All parameters from the MILS sensor, including gas flow, pressure, sample humidity, and internal temperature were logged to process and evaluate the quality of the data. A dedicated ship-mounted GPS logged positional data for accurate synchronization of the probe and ship position. A position correction, accounting for the lag between the probe and the ship synchronizes the towed instrument data with simultaneously acquired echosounder data. The Matlab routine "Mooring Design and Dynamics" (Dewey, 1999) simulated the towing scenario, for which we used a simplified instrument assembly composed by a cylinder 1.68 m long, 0.28 m diameter with a negative buoyancy of 52 kg, corresponding to the volume and buoyancy of the whole instrument assembly. A polynomial speed-factor ($x_* = -0.2211u^5 + 1.355u^4 - 3.0126u^3 + 2.6741u^2 - 0.1609u$) was derived to account for the combined ship- and water current velocities (u in m s^{-1}). The distance of the probe behind the ship and the corresponding required time-shift was calculated by multiplying the non-dimensional speed-factor (x_*) with the instrument depth at each data point. This approach allowed for dynamic correction of data positions, accounting for towing with or against the water current and a near-stationary ship during vertical profiling. Correction for tidal currents was neglected since tides constituted less than 5% of the WSC of ~0.2 m s^{-1} during our deployments, according to the tide model TPXO (Egbert and Erofeeva, 2002).

A time lag of 15 sec for the MILS was calculated based on the volume of the gas line between the extraction system and the measurement cell and the gas flow rate. We expect that concentrations profiles obtained from down- and up-casts align when this time lag is applied. The response time of the MILS is given by the flushing time of the measurement cell, and for this campaign, the T_{90} was 15 sec.

Mixing ratios of CH_4 (ppmv) measured by the MILS were converted into aqueous concentrations (nmol l^{-1}) using Henry's law, where the solubility coefficients were determined accordingly with Wiesenburg and Guinasso (1979), while accounting for in-situ pressure, temperature, and salinity. The uncertainty of the dissolved CH_4, measured with the MILS is ± 12% (Grilli et al., 2018).

2.4 Acoustic mapping and quantification of seafloor CH_4 emissions

Gas bubbles in the water column are efficient sound scatterers and ship-mounted echosounders can therefore be used for identifying and quantifying gas emissions (Weber et al., 2014;Veloso et al., 2015;Ostrovsky et al., 2008). The target strength (TS), defined as 10 times the 10-base logarithmic measurements of the frequency dependent acoustic cross sections (Medwin and Clay, 1997), quantifies the existence of sound scattering objects in the water column. Time series of TS are displayed in

so-called echograms (Greinert et al., 2006;Judd and Hovland, 2009). During the cruise, the 38 kHz channel of the ship-mounted single beam Simrad EK-60 echosounder recorded acoustic backscatter continuously. Flares can be identified in the echograms and distinguished from other acoustic scatter from fish schools, dense plankton aggregations, and strong water density gradients. We identify flares as features in echograms, which exceed the background backscatter by more than 10 dB, with a vertical extension larger than their horizontal, and which are attached to the seafloor.

We used the methodology developed and corrected by Veloso et al. (2015);Veloso et al. (2019a) and the prescribed FlareHunter software for mapping and quantifying gas release. For the flow rate calculations performed with the Flare Flow Module of FlareHunter, we used a bubble size spectra with a Gaussian distribution peaking at 3 mm equivalent radius, previously observed in the area (Veloso et al., 2015). Temperature, salinity, pressure, and sound velocities, all required for correct quantification, were provided by the CTD casts. The resulting flow rates and seepage positions allow for mass balance calculation in the control volume model and in the two-dimensional (2D) model, as described in Sect. 2.5 and 2.6, respectively.

2.5 Control volume model

The temporal evolution (dC/dt) of a solute's concentration C within a certain volume V, which is fixed in space, and with water flowing through it can, using mass conservation, be written as:

$$\frac{dC}{dt} = \frac{Q_{IN} \times C_B}{V} - \frac{Q_{OUT} \times C}{V} + \frac{F}{V} + k\nabla^2 C \tag{1}$$

Equation (1) is a second order differential equation, from which an analytical steady state solution can be derived by following these assumptions: The volumetric flow of water in and out of the control volume, Q_{IN} and Q_{OUT} are balanced and are given by a steady water current in the x-direction across the width (Δy) and height (Δz) of the control volume. The diffusion is kept homogenous and constant by applying a constant diffusion coefficient k. The background concentration C_B is fixed in time and space and F represents the persistent flow of the solute (in this case bubble mediated CH_4) into the volume. The CH_4 dissolves completely within the volume, and the diffusion occurs across the domain (in the y-direction). Using the central difference approximation of the second derivative (∇^2 in Eq. (1)) and the above assumptions yield that the aqueous CH_4 within the volume reaches the steady state concentration:

$$C_{t=\infty} = \left(\frac{Q_{IN} \times C_B}{V} + \frac{F}{V} + \frac{2k \times C_B}{(\Delta y)^2}\right) \times \left(\frac{Q_{OUT}}{V} + \frac{2k}{(\Delta y)^2}\right)^{-1} \tag{2}$$

Finally, by averaging measured CH_4 concentration within a defined volume, and assuming that it represents a steady state concentration, the bubble flow rate is retrieved from Eq. (2).

$$F = (\bar{C} - C_B) \times \left(Q + \frac{V \times 2k}{(\Delta y)^2}\right) \tag{3}$$

Where $\bar{C}$ represents the measured average concentration, and $Q = Q_{IN} = Q_{OUT}$.

The dimensions of the control volume with volume V = $\Delta x \times \Delta y \times \Delta z$, were chosen to match the length of line 3 (Δx = 4.5 km), extended 25 m perpendicularly on each side of the line (Δy = 50 m), and 75 m vertically (Δz = 75 m). A graphic describing the control volume is supplied in Fig. SI 1.

7

2.6 Two-dimensional model

In order to gain insight to the physical processes behind the observed CH_4 variability, we constructed a two-dimensional (2D)
numerical model, resolving the evolution of dissolved CH_4 in the water column, which results from CH_4-bubble emissions,
advection with water currents and diffusion. The model domain was made 400 m high in the z-direction, 4.5 km long in the x-
direction, and oriented along line 3 (Fig. 1a). The navigation data along this line is linearly interpolated to form the basis for a
2-metre gridded model domain starting at 78°34.54' N, 9°25.92' E and ending at 78°32.1' N, 9°30.58' E as indicated by N and
S, in Fig. 1a. FlareHunter derived flow rates within 50 m from line 3 were projected into the model domain, and the source of
dissolved CH_4, mediated by bubbles, was distributed vertically by applying a non-dimensional source-function similar to the
approach of Jansson et al. (2019): $S0(z) = 6.6 \times 10^{-2} \times e^{-0.066 \times z}$, where z is the vertical distance from the seafloor in metres.
We calculated source distribution functions $S(z)$ by scaling $S0(z)$ with the flare flow rates, and distributed the resulting source
into current-corrected x/z nodes with volumes $\delta V = \delta x \times \delta y \times \delta z$, where δx=δy=δz=2 m. The model domain comprises 12
extra cells on each side in the y-direction in order to avoid fast diffusion out of the domain while the background concentration
is held constant. The 2D model simulated CH_4 diffusion and advection with water currents, and was run to steady state using
different diffusion coefficients, within the range suggested by Sundermeyer and Ledwell (2001). A graphic representation of
the 2D model is shown in Fig. SI 1.

3 Results

3.1 Water properties

The measurements from the Seabird CTD during our survey indicates well-mixed water within 150 metres above the seafloor,
and continuously stratified water upwards to 50 metres below the sea level (mbsl) (Fig. 2a) with a squared buoyancy frequency
of ~$N^2 < 4 \times 10^{-5}$ s^{-2}. A pycnocline exists at ~30 mbsl (Fig. 2a) with N^2 up to 10^{-4} s^{-2}, marking the transition between surface
water and AW below (Fig. 2b and 2c). Temperatures close to the seafloor range from 4.2–4.4 °C, which is more than 1 °C
above the CH_4 hydrate stability limit (Tishchenko et al., 2005), for a salinity of 35.1 as indicated in Fig. 2a. The velocity of
the WSC was between 0.1 and 0.3 m s^{-1} (Fig. 2d) inferred from the inclination of flare spines (Veloso et al., 2015), which was
calculated from the echosounder data, obtained throughout the whole survey. The current followed the isobaths, which is
consistent with previous findings (Graves et al., 2015;Gentz et al., 2014). The mean salinity and temperature acquired with the
Andreaa CTD, in different layers, with their corresponding standard deviations according to the water masses classification
of Skogseth et al. (2005) and Ślubowska-Woldengen et al. (2007) are shown in Fig. 2b,c. The temperature/ salinity distribution
suggests a clear dominance of AW during the survey, overlaid with fresher and colder ASW and PW.
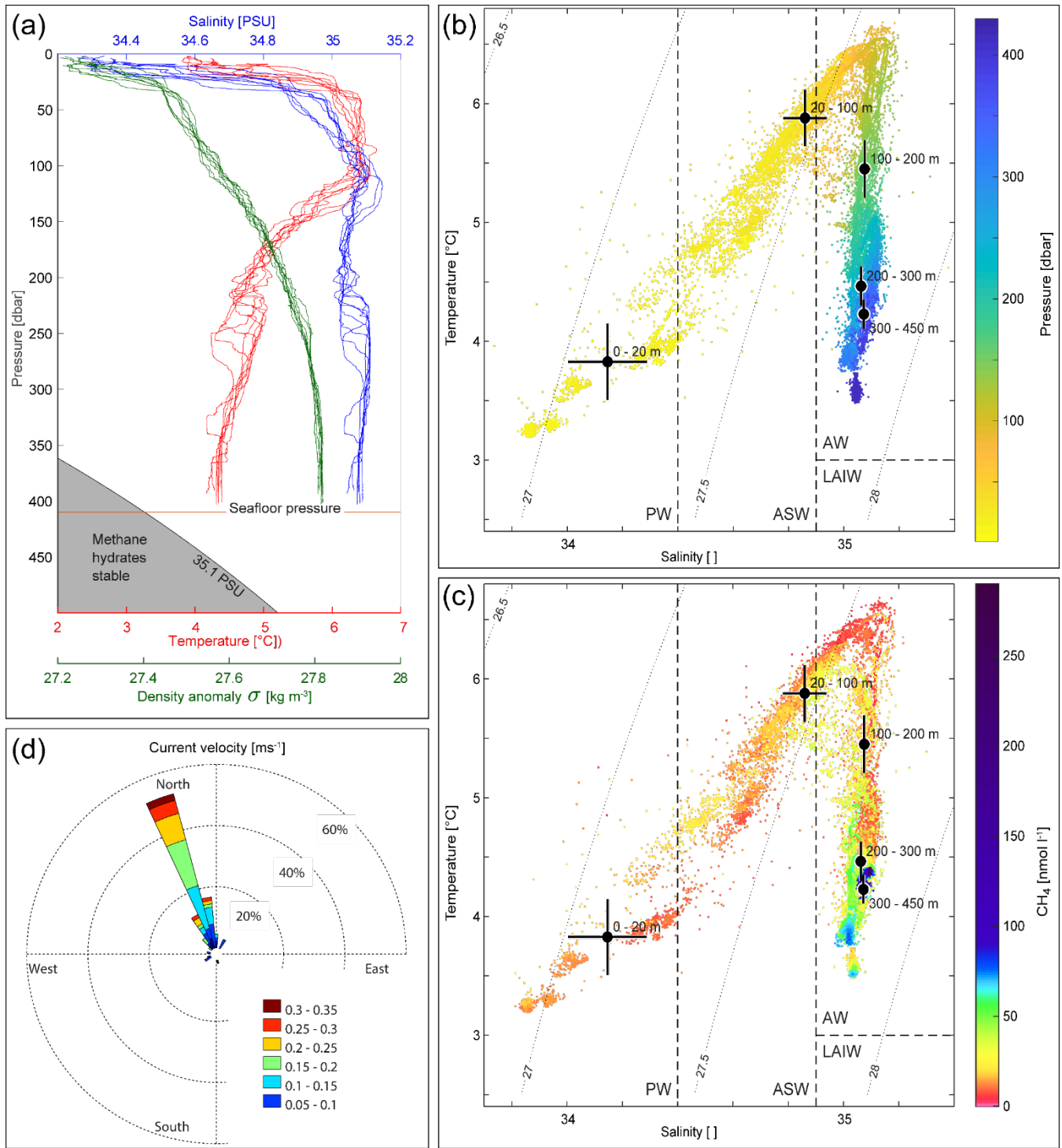
Figure 2. Hydrography during the survey. a) CTD casts 1617- 1626 showing temperature (red), salinity (blue) and density anomaly (green) calculated with Gibbs seawater package (McDougall and Barker, 2011). **b)** Temperature and salinity (TS) diagram coloured by pressure (dbar). Grey curved lines in the background indicate isopycnals (constant density (σ) lines). AW indicates Atlantic Water, PW is polar water, ASW is arctic surface water and LAIW is Lower Arctic Intermediate Water. Water mass definitions are described in the text. Black dots indicate the mean water properties for the different layers and crosses indicate the corresponding standard deviations. **c)** TS diagram coloured by CH_4 concentrations (nmol l^{-1}) measured with the MILS. Black dots depict average temperature and salinity at water depth intervals, and the error bars indicate the corresponding standard deviations. **d)** Water currents inferred from inclination of flare spines (Veloso et al., 2015) with a mean bubble rising speed of 23 cm s^{-1}.

3.2 Measured and modelled CH$_4$ distribution

The high-resolution dissolved CH_4 concentration profiles resulting from towing the MILS along five lines, approximately 15 meters above the seafloor (masf) show high variability (Fig. 3), especially over line 3, which geographically matches the clustering of bubble plumes (Fig. 1a).

9

225 On the landward side (lines 1 and 5), the concentration is relatively smooth with an average of ~55 nmol l^{-1}, but along line 5, which is closer to the main seepage area, the concentration is influenced by the nearby seepage, inferred from the concentration peaks reaching up to 105 nmol l^{-1} at 78°33.5' N. On the offshore side, the mean concentrations are 15 and 36 nmol l^{-1} along lines 4 and 2, respectively with elevated CH$_4$ concentrations of up to ~ 70 nmol l^{-1}, lacking hydroacoustic evidence of CH$_4$ seep sources. The peak in line 4 may be explained by its proximity to the main bubble seep cluster, but the CH$_4$ concentrations

230 show more variability along line 2, the offshore-most horizontal trajectory of the survey, which may indicate undetected CH$_4$ seepage located deeper than 400 mbsl.
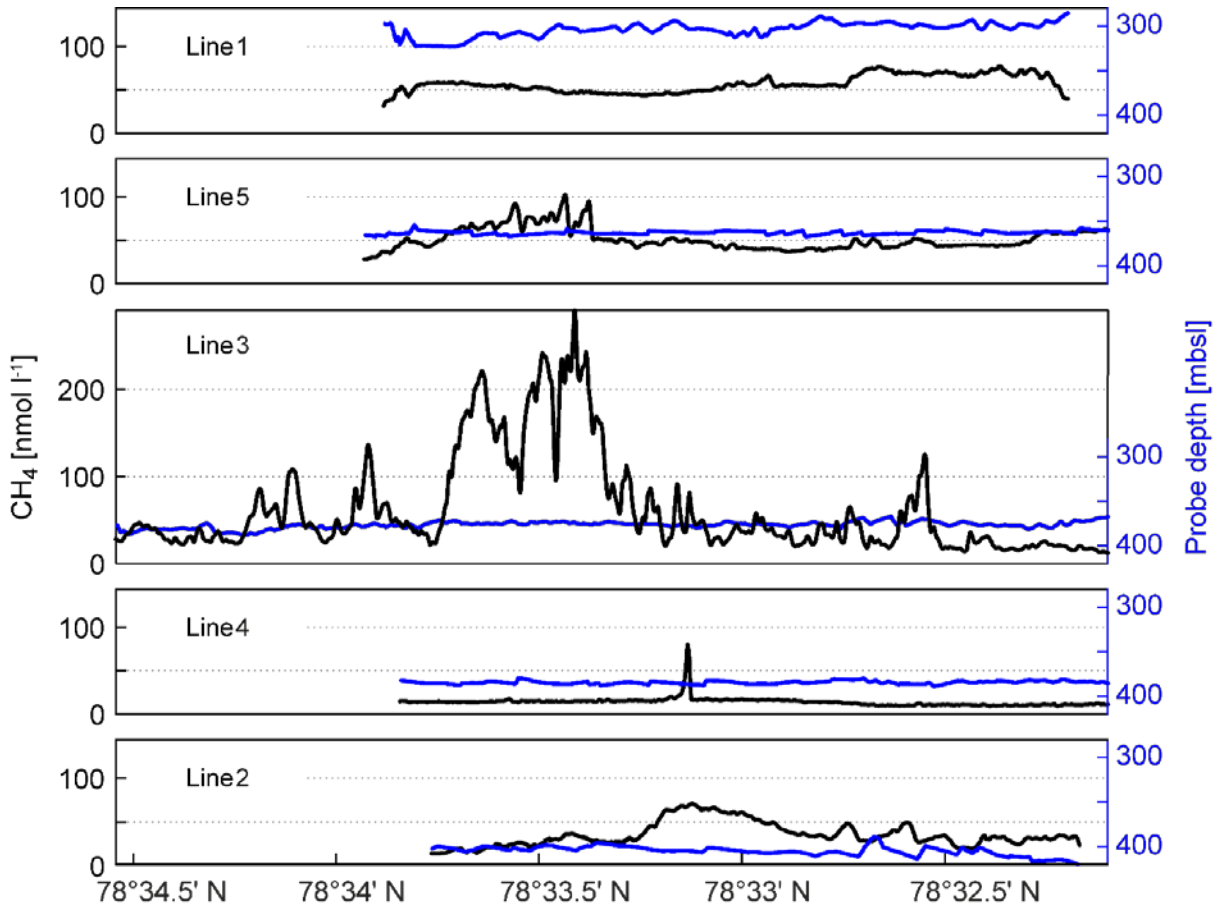
Figure 3. MILS measurements along the five lines ~15 m from the seafloor. Panels show data acquired along lines 1–5, shown in order of proximity to the shore, with line 1 closest to the shore and line 2 furthest offshore. See Fig. 1a for line locations. Black lines
235 **show CH$_4$ concentrations, blue lines show the probe depth.**

A 25-minute down- and upward sequence obtained from the vertical MILS cast at station 1616 (Fig. 4) shows excellent repeatability after correcting for the instrument time lag of 15 seconds. The sensor showed no memory effects, i.e. different response times between increased and decreased CH$_4$ concentrations.

Analysis of discrete samples (DS) from CTD casts 1618 and 1619 and the vertical MILS cast 1616 give further insights to the
240 heterogeneity and temporal variation of the dissolved CH$_4$ distribution (Fig. 4). Discrete measurements from CTDs 1618 and 1619 reveal a qualitative match with the MILS measured concentrations extracted from line 3 near these stations (red and green symbols in Fig. 4). Discrepancies between the MILS cast 1616 and the DS from CTDs 1618 and 1619 close to the

10

seafloor is likely due to the difference in sampling location, as the MILS vertical cast 1616 was ~150 and ~180 m away from CTDs 1618 and 1619, respectively.

245　The exponential "dissolution" function, which represents the expected trace of dissolved CH_4 in the water column, resulting from bubble dissolution, was compared to the entire MILS dataset by plotting CH_4 concentrations against height above the seafloor, determined from position corrected pressure and previously acquired multibeam data (Fig. 4).

Elevated CH_4 concentrations at ~160 and ~220 mbsl revealed by the MILS vertical profile 1616 was not identified with DS from the nearby CTD cast 1619, and DS from CTD 1618 reveal only a small fraction of the CH_4 anomaly, because of too

250　sparse sampling (Fig. 4). The MILS data collected 15 masf along line 3 reveals 50 nmol CH_4 l^{-1} while the vertical profile only 30 metres away (MILS-cast 1616), measured ~200 nmol CH_4 l^{-1} (Fig. 4). This emphasizes the strong spatiotemporal variability of the CH_4 distribution in the area.

Despite the high CH_4 variability in the horizontal profiles (Fig. 3), further analysis of the data may be obtained by focusing on line 3, towed in north-south direction at ~0.8 m s^{-1} directly over the bubble streams. Based on a mean depth of 390 m and the

255　depth of the towed CTD, the height above the seafloor of the towed probe along line 3, was 13.4 ± 3.8 m. The fast response time of the MILS sensor ($T_{90} = 15$ s) revealed decametre-scale variations of the dissolved CH_4 concentrations with high values well correlated with the echosounder signal, after correcting for the towed instrument position (Fig. 5).
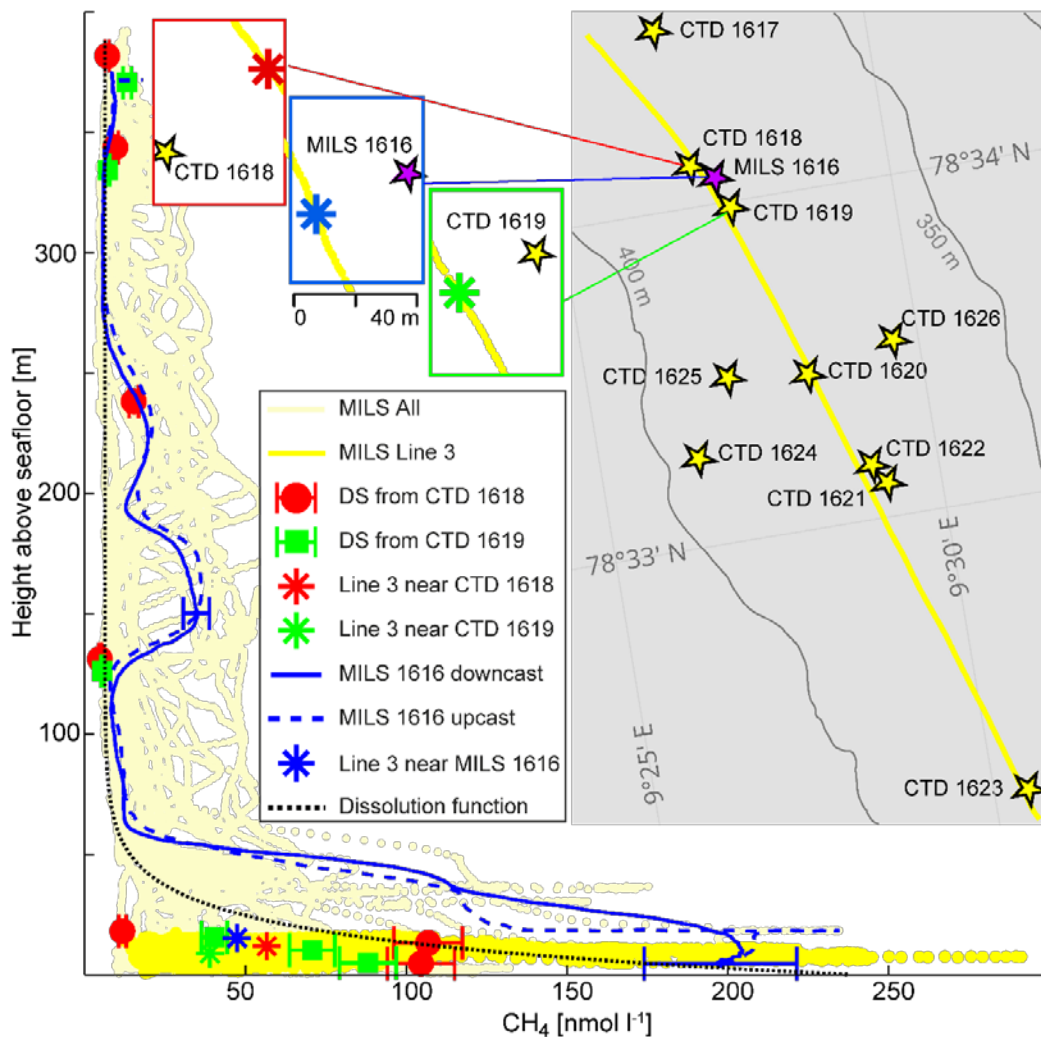
Figure 4. High-resolution CH₄ concentrations and discrete samples. Light yellow lines show CH₄ concentrations acquired with the MILS during the entire survey and the bright yellow derives from line 3 at ~15 masf only. Solid and dashed blue lines represent continuous down- and upward profiles acquired at station 1616 after correction for instrument response time. The blue error bars indicate the instrument uncertainty of 12%. Discrete sample data is shown as red dots (CTD 1618) and green squares (CTD 1619) with error bars that indicate the discrete sampling/ headspace GC method uncertainty of 4%. The asterisks indicate MILS data points from the towing along line 3, closest to the vertical cast 1616 (blue), to CTD 1618 (red) and CTD 1619 (green). The black dotted line indicates the exponential dissolution function described in the text. The inset map shows the locations of the CTDs with discrete sampling (stnr1617–1623) (yellow stars) as well as line 3, which is indicated with a yellow line. The blue rectangle shows the location of the vertical MILS profile from station 1616 (purple star) and the data point from line 3, which is closest to the deepest location of the vertical cast (blue asterisk). The green rectangle shows the location of CTD 1619 and the closest point on line 3 (green asterisk), while the red rectangle shows the location of CTD 1618 and the corresponding point on line 3 (red asterisk).
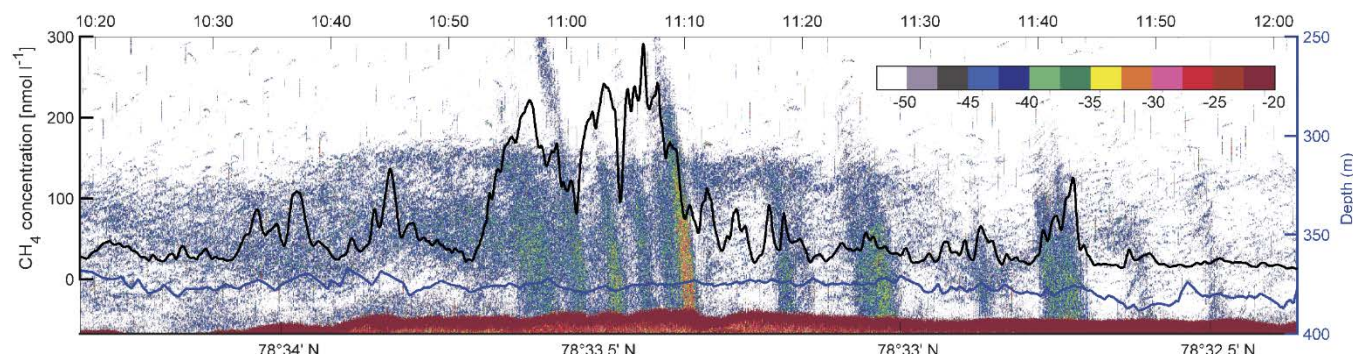

Figure 5. Towed MILS data overlying echo-sounder data. The black line shows the CH₄ concentration along line 3 (see Fig. 1 for location) at ~15 m from the seafloor. The blue line indicates the depth of the probe. The echogram, displaying TS values (colour bar shows intensity (-dB)) from the 38 kHz-channel of the EK60, is shown in the background.

A close analysis of the measured concentration reveals that the up- and down- stream gradients are equally distributed (bar chart in Fig. SI 2c). This symmetry suggests that CH₄ disperses fast and equally in all horizontal directions around the bubble plumes while being advected away from the source.

The measured CH₄ concentrations along line 3 changed significantly (5% or more) on sub-response times (<15 s) in only two instances and over a total time of 26 s, out of 1h 42 min, as indicated with red dots in Fig. SI 2a. This suggests that the MILS resolved 99.6% of the gradients and that the response time of the MILS did not limit the resolution of the CH₄ distribution. The mean absolute gradient, assessed from steadily increasing or decreasing concentrations (grey vertical lines in Fig. SI 2a show the position of the selected slopes), was 1.5 nmol l⁻¹ m⁻¹, corresponding to 1.2 nmol l⁻¹ s⁻¹. The minimum and maximum lateral gradients were -5.0, and 4.8 nmol l⁻¹ m⁻¹, which corresponds to -4.1 and 4.6 nmol l⁻¹ s⁻¹. Correlations of CH₄ concentrations versus depth and speed changes were low (R= 0.0133, -0.0001, -0.0094, 0.0028 for ship speed, ship acceleration, vertical instrument speed and instrument acceleration, respectively), showing the stability of the instrument during rapid movements and disproving artefacts due to water flow fluctuations at the membrane.

Sources of CH₄ constraining the control volume and 2D model were obtained from the acoustic mapping and quantification described in section 2.4. During the entire survey, we identified 68 unique groups of bubble plumes, with an average flow rate of 48 (SD = 50) ml min⁻¹. Within 50 metres of line 3, we acoustically identified 31 flares with an average flow rate of 60 (SD = 65) ml min⁻¹ amounting to a total flow rate of 1.87 l min⁻¹. These flow rates were taken as sources in the control volume and 2D model. FlareHunter calculates the flow rates in a layer 5–10 m above the seafloor. In order to calculate flow rates from the

12

seafloor, we upscaled the FlareHunter flow rates by 40% to compensate for bubble dissolution near the seafloor, in accordance with the dissolution profile.

The 2D model was run to steady state with different diffusion coefficients, $k \in [0.3 - 4.9 \text{ m}^2 \text{ s}^{-1}]$, adopted from dye-experiments offshore Rhode Island (Sundermeyer and Ledwell, 2001). These coefficients are in agreement with the ones obtained from the Celtic Sea ($k \in [0.8 - 4.4 \text{ m}^2 \text{ s}^{-1}]$) (Stashchuk et al., 2014), but much higher than the coefficient applied by Graves et al. (2015) ($k = 0.07 \text{ m}^2 \text{ s}^{-1}$). The best fit between the 2D model and the MILS data (R = 0.68) was achieved during a simulation with $k = 1.5 \text{ m}^2 \text{ s}^{-1}$. Because the high-end coefficients of Sundermeyer and Ledwell (2001) and Stashchuk et al. (2014) were derived during wavy conditions, and because our model mainly resolves the near-bottom region, away from wave action, we interpret that our best-fit diffusion coefficient is relatively high. The resulting range of model outputs and the best fit-model simulation are visualized and compared with high-resolution measurements in Fig. 6. Despite applying a high diffusion coefficient, the 2D model shows a residual downstream tailing, which is not seen in the MILS data. We attribute this to the fact that the model does not resolve small scale eddies, but only diffusion across the domain and diffusion/ advection along the domain.

The salinity and temperature profiles of the towed CTD indicate well-mixed water, particularly over the most prominent gas flares. Here, the relative standard deviation of the salinity and temperature drops by factors of 10, and 58 respectively, as highlighted by the dashed-line box in Fig. 6. The depth stability of the probe is also better in the area. Its relative standard deviation dropped by a factor of 3, which is not enough to justify the larger factors observed for the temperature and salinity. We interpret that this is caused by turbulent mixing enhanced by the bubble streams.
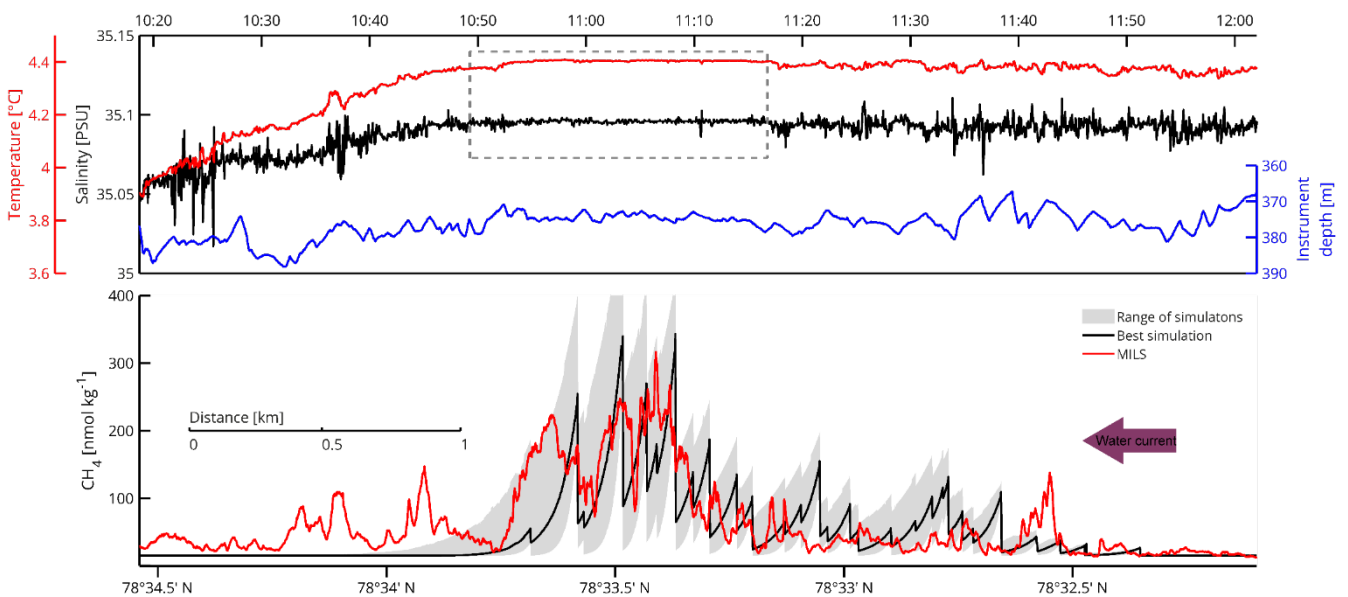
Figure 6. Water properties and comparison between modelled and measured dissolved CH₄ concentrations along line 3. Top panel shows temperature and salinity data together with the depth of the towed instruments. The dashed-line box highlights the area of intense mixing. In the lower panel, the red line shows the dissolved CH₄ measured by the MILS. The grey area indicates the range of CH₄ concentrations from the 2D model simulations. The black line depicts output of the model simulation with the best match with the measured concentrations.

13

3.3 Methane inventory

The method, dimensions, and resolution chosen for calculating CH_4 inventories may strongly influence the resulting content and average concentrations. This may have serious implications when the results are used for upscaling. To highlight this, we applied different inventory calculation methods on the same water volume.

320   Averages along line 3 were calculated from: a) Concentrations from discrete sampling, based on different sampling depths. b) Discrete data from different depths, linearly interpolated along the line. c) High-resolution data obtained from the MILS data ~15 masf. d) Concentrations extracted from the 2D model output at steady state at 15 masf.

Average concentrations were calculated in a "box" volume equivalent to MILS line 3 (4.5 km long (x-direction), 50 m wide (y-direction), equivalent to the echosounder beam width, 75 m high (z-direction) corresponding to the most dynamic and CH_4

325   enriched zone (e.g. McGinnis et al., 2006;Jansson et al., 2019;Graves et al., 2015). Box averages were derived as follows: The volume was divided into 1 m cubic cells. Cells located in the y-centre and in z-positions vertically matching the underlying data (DS or MILS) were populated with the MILS, or interpolated DS profiles. The remaining cells were populated by perpendicular and vertical extrapolation following the typical horizontal gradient of 1.5 nmol l^{-1} m^{-1}, and vertical dissolution profiles scaled by the measured or interpolated concentrations. The mean concentrations from the 2D model was delimited by

330   the height of the box. The control volume model provided only one value for the entire box.

The underlying data and its interpolation is seen in Fig. 7 and the resulting averages are reported in Table 1.
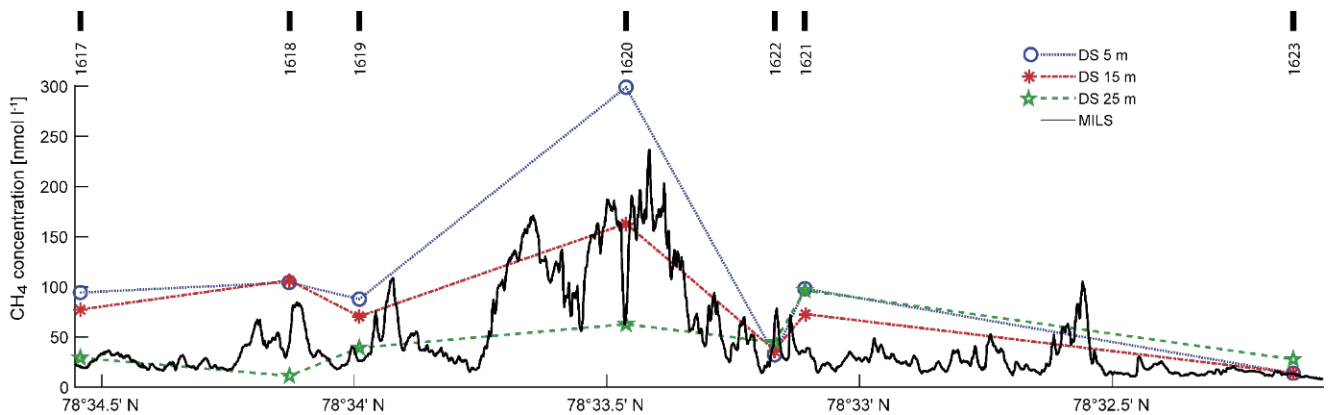
Figure 7: Underlying CH₄ concentration data for inventory calculations. Solid black line shows the continuous MILS profile ~15
335   **masf along line 3. DS concentrations at various depths are shown as blue circles, red asterisks and green stars for 5, 15 and 25 masf respectively, and blue dotted, red dash-dotted, and green dashed lines represent the corresponding linear horizontal interpolations. CTD cast numbers are marked with thick black lines at the top of the graph.**

The average CH_4 concentration in the box volume based on continuous data is similar to the average obtained from discrete data at 15 m above the seafloor. We obtained 47 vs 77 nmol l^{-1} for the high-resolution line and the interpolated DS, while the

340   box averages for the high-resolution and interpolated DS were 22 vs 29 nmol l^{-1}. The 2D model yielded a line average of 60 nmol l^{-1}, while it was 22 nmol l^{-1} for the box. The control volume model predicted a steady state concentration of 23 nmol l^{-1} when the diffusion coefficient of 1.5 m^2 s^{-1}, inferred from the 2D model was applied.

14

4 Discussion

During our survey, the mean flow rate at the seafloor per flare within 50 m of line 3, was 84 (SD = 91.6) ml min^{-1}, (min = 15.8, max= 355.6 ml min^{-1}). This is comparable with the flow rate per flare of 125 ml min^{-1}, estimated by Sahling et al. (2014) who assumed that an acoustic flare consists of 6 bubble streams, each with a flow rate of 20.9 ml min^{-1}. The authors found 452 flares in the area, for which they assumed similar flow rates, and thereby calculated a total flow in the area of ~57 l min^{-1}. Our study encompasses a smaller area, where we only detected 68 flares (31 flares within 50 m of line 3) and the total flow rate from these 68 flares was 4.56 l min^{-1}. This total flow translates to 65.7 t CH_4 y^{-1} assuming constant ebullition. Considering the sparse beam coverage and relatively small area, this may be compared to CH_4 seepage of ~550 t CH_4 y^{-1} estimated for a larger area, covered by 9 surveys (Veloso et al., 2019b), and ~400 t CH_4 y^{-1} (Sahling et al., 2014), in a study area covering ours, but also extending northwards, where additional gas venting occurs. A comparison of studies from the same area, using different methods, shows a large range of yearly CH_4 emissions to the water column. Flow rates of CH_4 per distance along the continental shelf from previous studies given by the authors (900 kg m^{-1} y^{-1} (Westbrook et al., 2009); 141 kg m^{-1} y^{-1} (Reagan et al., 2011); 13.8 (6.9–20.6) t m^{-1} y^{-1} (Marín-Moreno et al., 2013); 2400 (400–4500) mol m^{-1} y^{-1} (Sahling et al., 2014); 748 (561–935) t m^{-1} y^{-1} (Berndt et al., 2014)) yield emissions of 4050, 635, 992, 173 and 54000 t CH_4 y^{-1} over the 4500 m section of the continental shelf which corresponds to our line 3.

The MILS data collected 15 masf along line 3 did not reveal the high concentrations (~200 nmol l^{-1}) measured during the vertical cast only 30 m away, emphasizing the heterogeneous CH_4 distribution, and highlighting the need for high-resolution sensing, rather than sparse discrete sampling.

The fast response of the MILS helped revealing decametre scale variability of dissolved CH_4, and we conclude that uncertainties introduced by MILS response time were negligible in this survey. The observed symmetry of CH_4 gradients suggests fast dispersion in all horizontal directions while enriched water is advected away from the sources.

Because the instrument assembly lacked an inertia measurement unit, the stability during towing is unknown, but we did not observe any effect on the measurements from wobble and/ or rotation.

Gentz et al. (2014) and Myhre et al. (2016) suggested that a pronounced pycnocline is a prerequisite to limit the vertical transport of dissolved CH_4 towards the surface. One should note that this hypothesis was based on discrete sample data, rather than high-resolution data. We observed high CH_4 concentrations up to 75–100 masf, which is in agreement with bubble models (e.g. McGinnis et al., 2006;Jansson et al., 2019), highlighting that bubbles of observed sizes (~3 mm average equivalent radius) are fully dissolved within this range. Density stratification plays an important role in the vertical distribution of dissolved CH_4 because turbulent energy is required to mix solvents across isopycnals. Vertical mixing is therefore inhibited even without the presence of a strong pycnocline. We suggest that the observed height limit is a result of rapid bubble dissolution and inefficient vertical mixing, regardless of the existence of a pronounced pycnocline.

We observed CH_4 concentrations of up to 100 nmol l^{-1} without the acoustic signature of flares north of the active flare zone

375   (Fig. 5). Echograms from the CAGE 15-6 survey (this work) and previous surveys conducted in 2010 (AOEM 2010 cruise, University of Tromsø, with RV Jan Mayen) and 2013 (CAGE 13-7 cruise, with RV Helmer Hanssen (e.g. Portnov et al., 2016)) reveal that the nearest bubble stream is located ~300 m northeast of this CH_4 anomaly. Several hypotheses may explain this CH_4 enrichment: a) nearby presence of CH_4 enriched water seepage (hypothetically from dissociating hydrates) from the seafloor; b) presence of bubble streams with bubbles too small to be detected by the echosounder (the detection limit (TS<-60

380   dB) of a single bubble was 0.42 mm for this survey); c) advection of CH_4-enriched water from an upstream bubble plume source, not detected by the echosounder. In our case, the temperature- and salinity anomaly, which coincides with the increased CH_4, reveals mixing of AW with colder and fresher water (Fig. 6). Because mixing lines drawn in the TS diagrams (Fig. 2b and 2c) point towards PW rather than a pure fresh water source, our data supports hypothesis c, namely that AW mixed with PW was transported, and enriched in CH_4 while passing over a bubble plume before reaching the location of the measurement.

385   Lateral eddies or bottom Ekman transport may have been responsible for the intrusion of fresh, cold, CH_4 enriched water.

The 2D model relies on acoustically detected bubble plume locations, and the difference between measured and modelled CH_4 is obvious along line 3 from 10:30 to 10:50 as seen in Fig. 6. The CH_4 signal from high-resolution data, not thoroughly resolved by the model, underscores that mapping and modelling based on echosounder data are not enough for a correct quantitative estimate of the CH_4 inventory. The 2D model required a high diffusion coefficient in order to reproduce the variability of

390   measurements, which is supported by high turbulence in the area, caused by the strong currents. Downstream tailing of CH_4 concentrations seen in the 2D model was not observed with the MILS. In fact, MILS data reveal equal distribution of down- and upstream concentration gradients. We explain the discrepancy by the fact that the 2D model does not resolve eddies and the CH_4 source is placed in discrete cells, following a theoretical straight bubble line, and not accounting for diffusion along the bubble paths.

395   The relatively high midwater (120–260 mbsl) CH_4 concentrations revealed by the vertical MILS cast 1616 was only partly observed in the discrete sampling and was not inferred from echosounding. We suggest that this discrepancy is attributed to seepages at the corresponding depth interval, not previously mapped. The closest known seepages are a few km away from the location, at the shallow shelf (50–150 mbsl) and at the shelf-break (~250 mbsl) (Veloso et al., 2015), but it is doubtful that water masses from these locations can reach the surveyed area, as the WSC is persistently northbound. Unless horizontal

400   eddies transport CH_4 from the shelf-break to this area, this result indicates the existence of undiscovered CH_4 bubble plumes further south, at the depth of the observed anomaly.

The high-resolution data from the MILS results in a significantly lower CH_4 inventory than the one obtained from discrete sampling (47 vs 77 nmol l^{-1}) due to the heterogeneous distribution of dissolved CH_4. The choice of discrete sample locations can significantly affect the resulting average concentration. The average CH_4 concentration (93 nmol l^{-1}) estimated by

405   Graves et al. (2015) from a box with dimensions $\Delta x = 1m$, $\Delta y = 50$ m, $\Delta z = 75$ m, obtained from a DS transect across the

16

slope, was substantially higher than our box estimates of 20–39 nmol l^{-1}. These two results highlight the need for high-resolution sensing when estimating CH$_4$ inventories and average CH$_4$ concentrations.

The optical spectrometer of the MILS can be tuned or replaced to improve its sensitivity or to sample more CH$_4$ enriched waters. We believe the MILS would be an excellent tool for evaluating CH4 related water column processes. Grilli et al. (2018) reported a sensitivity of ±25 ppbv in air, which translates to ±0.03 nmol l^{-1} at 20 °C and a salinity of 38, which is low enough for investigations of atmospheric exchange and CH4 production/ consumption rates.

5 Conclusion

We have presented new methods for understanding the dynamics of CH$_4$ after its release from the seafloor, coupling for the first time continuous high-resolution measurements from a reliable and fast CH$_4$ sensor (MILS) with dedicated models. The MILS sensor was successfully deployed as a towed body from a research vessel and provided high-resolution, real-time data of both vertical and horizontal dissolved CH$_4$ distribution in an area of intense seepage west of Svalbard. For the first time, we observed a more heterogeneous CH$_4$ distribution than has been previously presumed.

We employed an inverse acoustic model for CH$_4$ seepage mapping and quantification, which provided the basis for a new 2D model and a new control volume model, which both agreed relatively well with observations. The 2D model did not reproduce the symmetric gradients observed with the MILS, which suggests a need to improve the model by including turbulent mixing enhanced by the bubbles streams.

Despite the large spatial and temporal variability of the CH$_4$ concentrations, a comparison between high-resolution (MILS) and DS data showed good general agreement between the two methods.

Heterogeneous CH$_4$ distribution measured by MILS matched acoustic backscatter, except for an area with high CH$_4$ concentrations without acoustic evidence of CH$_4$ source. Similarly, high midwater CH$_4$ concentration was observed by the MILS vertical casts with little evidence of a nearby CH$_4$ source, further supporting that high-resolution sensing is an essential tool for accurate CH$_4$ inventory assessment and that high-resolution sensing can give clues to undetected sources.

CH$_4$ inventories, given by discrete sampling agreed with those from high-resolution measurements, but sparse sampling may over- or underestimate inventories, which may have repercussions if the acquired data is used for predicting degassing of CH$_4$ to the atmosphere in climate models. The added detail of the fine structure allows for better inventories, elucidates the heterogeneity of the dissolved gas, and provides a better insight to the physical processes that influence the CH$_4$ distribution. The methods for understanding CH$_4$ seepage presented here shows potential for improved detection and quantification of dissolved gas in oceans and lakes. Applications for high-resolution CH$_4$ sensing with the MILS include environmental and climate studies as well as gas leakage detection desired by fossil fuel industry.

17

6 Data availability

A dataset comprising the MILS sensor data and echosounder files is available from the UiT Open Research Data repository https://doi.org/10.18710/UWP6LL.

7 Author contribution

PJ and JT contributed equally to the work leading to this manuscript, and are listed alphabetically. JM and JC initiated the collaboration and designed the study. JT, RG, PJ, and JM planned and participated in the field campaign. JT and RG systematized and synchronized the high-resolution MILS data. PJ mapped and quantified gas seepage and water currents by collecting and analysing echosounder data. PJ collected and analysed the CTD data and water samples, and organized the data repository. RG converted mixing ratios to aqueous concentrations. PJ developed the numerical models. AS analysed the water mass properties. JT and PJ calculated CH_4 inventories. All authors contributed to the manuscript.

8 Acknowledgements

References

Andreassen, K., Hubbard, A., Winsborrow, M., Patton, H., Vadakkepuliyambatta, S., Plaza-Faverola, A., Gudlaugsson, E., Serov, P., Deryabin, A., Mattingsdal, R., Mienert, J., and Bünz, S.: Massive blow-out craters formed by hydrate-controlled methane expulsion from the Arctic seafloor, Science, 356, 948, 10.1126/science.aal4500, 2017.

Berndt, C., Feseker, T., Treude, T., Krastel, S., Liebetrau, V., Niemann, H., Bertics, V. J., Dumke, I., Dünnbier, K., Ferré, B., Graves, C., Gross, F., Hissmann, K., Hühnerbach, V., Krause, S., Lieser, K., Schauer, J., and Steinle, L.: Temporal Constraints on Hydrate-Controlled Methane Seepage off Svalbard, Science, 343, 284, 10.1126/science.1246298, 2014.

Biastoch, A., Treude, T., Rüpke, L. H., Riebesell, U., Roth, C., Burwicz, E. B., Park, W., Latif, M., Böning, C. W., and Madec, G.: Rising Arctic Ocean temperatures cause gas hydrate destabilization and ocean acidification, Geophysical Research Letters, 38, 10.1029/2011GL047222, 2011.

Boetius, A., and Wenzhöfer, F.: Seafloor oxygen consumption fuelled by methane from cold seeps, Nature Geoscience, 6, 725-734, 10.1038/ngeo1926, 2013.

Boulart, C., Prien, R., Chavagnac, V., and Dutasta, J.-P.: Sensing Dissolved Methane in Aquatic Environments: An Experiment in the Central Baltic Sea Using Surface Plasmon Resonance, Environmental Science & Technology, 47, 8582-8590, 10.1021/es4011916, 2013.

Boulart, C., Briais, A., Chavagnac, V., Révillon, S., Ceuleneer, G., Donval, J.-P., Guyader, V., Barrere, F., Ferreira, N., Hanan, B., Hémond, C., Macleod, S., Maia, M., Maillard, A., Merkuryev, S., Park, S.-H., Ruellan,

E., Schohn, A., Watson, S., and Yang, Y.-S.: Contrasted hydrothermal activity along the South-East Indian Ridge (130°E–140°E): From crustal to ultramafic circulation, Geochemistry, Geophysics, Geosystems, 18, 2446-2458, 10.1002/2016GC006683, 2017.

Damm, E., Mackensen, A., Budéus, G., Faber, E., and Hanfland, C.: Pathways of methane in seawater: Plume spreading in an Arctic shelf environment (SW-Spitsbergen), Continental Shelf Research, 25, 1453-1472, 10.1016/j.csr.2005.03.003, 2005.

Dewey, R. K.: Mooring Design & Dynamics—a Matlab® package for designing and analyzing oceanographic moorings, Marine Models, 1, 103-157, 10.1016/S1369-9350(00)00002-X, 1999.

Egbert, G. D., and Erofeeva, S. Y.: Efficient Inverse Modeling of Barotropic Ocean Tides, Journal of Atmospheric and Oceanic Technology, 19, 183-204, 10.1175/1520-0426(2002)019<0183:EIMOBO>2.0.CO;2, 2002.

Ferré, B., Mienert, J., and Feseker, T.: Ocean temperature variability for the past 60 years on the Norwegian-Svalbard margin influences gas hydrate stability on human time scales, Journal of Geophysical Research: Oceans (1978–2012), 117, 10.1029/2012JC008300, 2012.

Gentz, T., Damm, E., Schneider von Deimling, J., Mau, S., McGinnis, D. F., and Schlüter, M.: A water column study of methane around gas flares located at the West Spitsbergen continental margin, Continental Shelf Research, 72, 107-118, 10.1016/j.csr.2013.07.013, 2014.

Graves, C. A., Steinle, L., Rehder, G., Niemann, H., Connelly, D. P., Lowry, D., Fisher, R. E., Stott, A. W., Sahling, H., and James, R. H.: Fluxes and fate of dissolved methane released at the seafloor at the landward limit of the gas hydrate stability zone offshore western Svalbard, Journal of Geophysical Research: Oceans, 120, 6185-6201, 10.1002/2015JC011084, 2015.

Greinert, J., Artemov, Y., Egorov, V., De Batist, M., and McGinnis, D.: 1300-m-high rising bubbles from mud volcanoes at 2080m in the Black Sea: Hydroacoustic characteristics and temporal variability, Earth and Planetary Science Letters, 244, 1-15, 10.1016/j.epsl.2006.02.011, 2006.

Grilli, R., Triest, J., Chappellaz, J., Calzas, M., Desbois, T., Jansson, P., Guillerm, C., Ferré, B., Lechevallier, L., Ledoux, V., and Romanini, D.: Sub-Ocean: Subsea Dissolved Methane Measurements Using an Embedded Laser Spectrometer Technology, Environmental Science & Technology, 52, 10543-10551, 10.1021/acs.est.7b06171, 2018.

Hong, W. L., Torres, M. E., Portnov, A., Waage, M., Haley, B., and Lepland, A.: Variations in Gas and Water Pulses at an Arctic Seep: Fluid Sources and Methane Transport, Geophysical Research Letters, 45, 4153-4162, 10.1029/2018GL077309, 2018.

Jansson, P., Ferré, B., Silyakova, A., Dølven, K. O., and Omstedt, A.: A new numerical model for understanding free and dissolved gas progression toward the atmosphere in aquatic methane seepage systems, Limnology and Oceanography: Methods, 0, doi:10.1002/lom3.10307, 2019.

Judd, A., and Hovland, M.: Seabed fluid flow: the impact on geology, biology and the marine environment, Cambridge University Press, 2009.

Jørgensen, N. O., Laier, T., Buchardt, B., and Cederberg, T.: Shallow hydrocarbon gas in the nothern Jutland-Kattegat region, Denmark, Bull. Geol. Soc, 38, 69-76, 1990.

Loeng, H.: Features of the physical oceanographic conditions of the Barents Sea, Polar Research, 10, 5-18, 10.3402/polar.v10i1.6723, 1991.

Marín-Moreno, H., Minshull Timothy, A., Westbrook Graham, K., Sinha, B., and Sarkar, S.: The response of methane hydrate beneath the seabed offshore Svalbard to ocean warming during the next three centuries, Geophysical Research Letters, 40, 5159-5163, 10.1002/grl.50985, 2013.

McDougall, T. J., and Barker, P. M.: Getting started with TEOS-10 and the Gibbs Seawater (GSW) oceanographic toolbox, SCOR/IAPSO WG, 127, 1-28, 2011.

McGinnis, D., Greinert, J., Artemov, Y., Beaubien, S., and Wüest, A.: Fate of rising methane bubbles in stratified waters: How much methane reaches the atmosphere?, Journal of Geophysical Research: Oceans (1978–2012), 111, 10.1029/2005JC003183, 2006.

Medwin, H., and Clay, C. S.: Fundamentals of acoustical oceanography, Academic press, 1997.

Miller, C. M., Dickens, G. R., Jakobsson, M., Johansson, C., Koshurnikov, A., O'Regan, M., Muschitiello, F., Stranne, C., and Mörth, C. M.: Pore water geochemistry along continental slopes north of the East Siberian Sea: inference of low methane concentrations, Biogeosciences, 14, 2929-2953, 10.5194/bg-14-2929-2017, 2017.

Myhre, C. L., Ferré, B., Platt, S. M., Silyakova, A., Hermansen, O., Allen, G., Pisso, I., Schmidbauer, N., Stohl, A., and Pitt, J.: Extensive release of methane from Arctic seabed west of Svalbard during summer 2014 does not influence the atmosphere, Geophysical Research Letters, 43, 4624-4631, 10.1002/2016GL068999, 2016.

Ostrovsky, I.: Methane bubbles in Lake Kinneret: Quantification and temporal and spatial heterogeneity, Limnology and Oceanography, 48, 1030-1036, 10.4319/lo.2003.48.3.1030, 2003.

530 Ostrovsky, I., McGinnis, D. F., Lapidus, L., and Eckert, W.: Quantifying gas ebullition with echosounder: the role of methane transport by bubbles in a medium-sized lake, Limnology and Oceanography: Methods, 6, 105-118, 10.4319/lom.2008.6.105, 2008.

Platt, S. M., Eckhardt, S., Ferré, B., Fisher, R. E., Hermansen, O., Jansson, P., Lowry, D., Nisbet, E. G., Pisso, I., Schmidbauer, N., Silyakova, A., Stohl, A., Svendby, T. M., Vadakkepuliyambatta, S., Mienert, J., and Lund

535 Myhre, C.: Methane at Svalbard and over the European Arctic Ocean, Atmos. Chem. Phys., 18, 17207-17224, 10.5194/acp-18-17207-2018, 2018.

Pohlman, J. W., Greinert, J., Ruppel, C., Silyakova, A., Vielstädte, L., Casso, M., Mienert, J., and Bünz, S.: Enhanced CO<sub>2</sub> uptake at a shallow Arctic Ocean seep field overwhelms the positive warming potential of emitted methane, Proceedings of the National Academy of Sciences, 114, 5355,

540 10.1073/pnas.1618926114, 2017.

Portnov, A., Vadakkepuliyambatta, S., Mienert, J., and Hubbard, A.: Ice-sheet-driven methane storage and release in the Arctic, Nature communications, 7, 10314, 2016.

Reagan, M. T., Moridis, G. J., Elliott, S. M., and Maltrud, M.: Contribution of oceanic gas hydrate dissociation to the formation of Arctic Ocean methane plumes, Journal of Geophysical Research: Oceans, 116,

545 10.1029/2011JC007189, 2011.

Reeburgh, W. S.: Oceanic Methane Biogeochemistry, Chemical Reviews, 107, 486-513, 10.1021/cr050362v, 2007.

Ruppel, C. D., and Kessler, J. D.: The Interaction of Climate Change and Methane Hydrates, Reviews of Geophysics, 10.1002/2016RG000534, 2016.

550 Sahling, H., Römer, M., Pape, T., Bergès, B., dos Santos Fereirra, C., Boelmann, J., Geprägs, P., Tomczyk, M., Nowald, N., and Dimmler, W.: Gas emissions at the continental margin west of Svalbard: mapping, sampling, and quantification, Biogeosciences, 11, 6029-6046, 10.5194/bg-11-6029-2014, 2014.

Schauer, U., Fahrbach, E., Osterhus, S., and Rohardt, G.: Arctic warming through the Fram Strait: Oceanic heat transport from 3 years of measurements, Journal of Geophysical Research: Oceans, 109, 10.1029/2003JC001823,

555 2004.

Shakhova, N., Semiletov, I., Salyuk, A., Yusupov, V., Kosmach, D., and Gustafsson, Ö.: Extensive Methane Venting to the Atmosphere from Sediments of the East Siberian Arctic Shelf, Science, 327, 1246-1250, 10.1126/science.1182221, 2010.

Shakhova, N., Semiletov, I., Leifer, I., Sergienko, V., Salyuk, A., Kosmach, D., Chernykh, D., Stubbs, C.,

560 Nicolsky, D., Tumskoy, V., and Gustafsson, O.: Ebullition and storm-induced methane release from the East Siberian Arctic Shelf, Nature Geosci, 7, 64-70, 10.1038/ngeo2007, 2014.

Skogseth, R., Haugan, P. M., and Jakobsson, M.: Watermass transformations in Storfjorden, Continental Shelf Research, 25, 667-695, 10.1016/j.csr.2004.10.005, 2005.

Ślubowska-Woldengen, M., Rasmussen, T. L., Koç, N., Klitgaard-Kristensen, D., Nilsen, F., and Solheim, A.:

565 Advection of Atlantic Water to the western and northern Svalbard shelf since 17,500calyr BP, Quaternary Science Reviews, 26, 463-478, 10.1016/j.quascirev.2006.09.009, 2007.

Sommer, S., Schmidt, M., and Linke, P.: Continuous inline mapping of a dissolved methane plume at a blowout site in the Central North Sea UK using a membrane inlet mass spectrometer – Water column stratification impedes immediate methane release into the atmosphere, Marine and Petroleum Geology, 68, 766-775,

570 10.1016/j.marpetgeo.2015.08.020, 2015.

Stashchuk, N., Vlasenko, V., Inall, M. E., and Aleynik, D.: Horizontal dispersion in shelf seas: High resolution modelling as an aid to sparse sampling, Progress in Oceanography, 128, 74-87, 10.1016/j.pocean.2014.08.007, 2014.

Steinle, L., Graves, C. A., Treude, T., Ferré, B., Biastoch, A., Bussmann, I., Berndt, C., Krastel, S., James, R. H.,

575 Behrens, E., Böning, C. W., Greinert, J., Sapart, C.-J., Scheinert, M., Sommer, S., Lehmann, M. F., and Niemann, H.: Water column methanotrophy controlled by a rapid oceanographic switch, Nature Geoscience, 8, 378, 10.1038/ngeo2420, 2015.

Sundermeyer, M. A., and Ledwell, J. R.: Lateral dispersion over the continental shelf: Analysis of dye release experiments, Journal of Geophysical Research: Oceans, 106, 9603-9621, 10.1029/2000JC900138, 2001.

580 Tishchenko, P., Hensen, C., Wallmann, K., and Wong, C. S.: Calculation of the stability and solubility of methane hydrate in seawater, Chemical geology, 219, 37-52, 10.1016/j.chemgeo.2005.02.008, 2005.

Veloso, M., Greinert, J., Mienert, J., and De Batist, M.: A new methodology for quantifying bubble flow rates in deep water using splitbeam echosounders: Examples from the Arctic offshore NW-Svalbard, Limnology and Oceanography: Methods, 13, 267-287, 10.1002/lom3.10024, 2015.

585 Veloso, M., Greinert, J., Mienert, J., and De Batist, M.: Corrigendum: A new methodology for quantifying bubble flow rates in deep water using splitbeam echosounders: Examples from the Arctic offshore NW-Svalbard, Limnology and Oceanography: Methods, 17, 177-178, 10.1002/lom3.10313, 2019a.

Veloso, M., Jansson, P., De Batist, M., Minshull, T. A., Westbrook, G. K., Pälike, H., Bünz, S., Wright, I., and Greinert, J.: Variability of acoustically evidenced methane bubble emissions offshore western Svalbard, Geophysical Research Letters, 10.1029/2019GL082750 2019b.

590

Wankel, S. D., Joye, S. B., Samarkin, V. A., Shah, S. R., Friederich, G., Melas-Kyriazi, J., and Girguis, P. R.: New constraints on methane fluxes and rates of anaerobic methane oxidation in a Gulf of Mexico brine pool via in situ mass spectrometry, Deep Sea Research Part II: Topical Studies in Oceanography, 57, 2022-2029, 10.1016/j.dsr2.2010.05.009, 2010.

595

Weber, T. C., Mayer, L., Jerram, K., Beaudoin, J., Rzhanov, Y., and Lovalvo, D.: Acoustic estimates of methane gas flux from the seabed in a 6000 km2 region in the Northern Gulf of Mexico, Geochemistry, Geophysics, Geosystems, 15, 1911-1925, 10.1002/2014GC005271, 2014.

Westbrook, G. K., Thatcher, K. E., Rohling, E. J., Piotrowski, A. M., Pälike, H., Osborne, A. H., Nisbet, E. G., Minshull, T. A., Lanoisellé, M., and James, R. H.: Escape of methane gas from the seabed along the West

600

Spitsbergen continental margin, Geophysical Research Letters, 36, 10.1029/2009GL039191, 2009.

Wiesenburg, D. A., and Guinasso, J. N. L.: Equilibrium solubilities of methane, carbon monoxide, and hydrogen in water and sea water, Journal of Chemical and Engineering Data, 24, 356-360, 10.1021/je60083a006, 1979.

21

Table 1: Average concentrations (nmol l^{-1}) calculated with different methods at different altitudes as indicated in the first column (metres above the seabed, masf). [1]Average of the sparse discrete sampling. [2]Average of high-resolution (MILS) measurements. [3]Average of linearly interpolated concentrations based on discrete measurements. [4]Average concentrations from the 2D model, extracted from depths matching the MILS position. [5]Average concentrations within the box (4500 m (L) × 50 m (W) × 75 m (H)) based on the high-resolution measurements or interpolated concentrations along the box, the vertical dissolution-profile, and the mean horizontal concentration gradient across the width of the box. [6]Average of the 2D model best simulation result from 0–75 masf. [7]The CV model yields a box value only.

Dataset	Discrete	High-resolution	Box
MILS ~15 masf	-	47[2]	22[5]
DS ~5 masf	104[1]	108[3]	39[5]
DS ~15 masf	77[1]	77[3]	29[5]
DS ~25 masf	44[1]	49[3]	20[5]
2D model (~15[4] and 0–75[6] masf)	-	60[4]	22[6]
CV model	-	-	23[7]